minerals

MDPI

Article

Fracture Fillings and Implication of Fluid Activities in Volcanic Rocks: Dixi Area in Kelameili Gas Field, Junggar Basin, Northwestern China

Mingyou Feng [1], Tian Liu [1], Tong Lin [2], Xiaohong Liu [1,*], Ningxin Li [1] and Aihua Xi [1]

[1] School of Geoscience and Technology, Southwest Petroleum University, Chengdu 610500, China; fmyswpu@163.com (M.F.); liutian0228@163.com (T.L.); linxws@163.com (N.L.); aihuaxi@163.com (A.X.)

[2] Research Institute of Petroleum Exploration and Development, PetroChina, Beijing 100083, China; lintong69@petrochina.com.cn

* Correspondence: 200831010021@swpu.edu.cn

Received: 15 December 2018; Accepted: 25 February 2019; Published: 3 March 2019

Abstract: The Carboniferous Batamayineishan Formation of the Kelameili Gas Field is a specific weathered crust-related volcanic reservoir that has a significant production rate in the Junggar Basin, Northwestern China, attributed to debatable processes of fluid evolution. The results suggest that various types of fluids occurring in volcanic rocks lead to the filling of quartz and calcite in fractures and their associated alteration haloes. The silica that formed quartz veins was mainly derived from deep hydrothermal fluids, while the carbon dioxide that formed calcite veins originated from sources characterized by mixing and alteration of deep hydrothermal and hydrocarbon fluids. Siliceous hydrothermal fluids rich in sulphur dioxide and other volatile components were driven by a pressure gradient and buoyancy, and circulated both laterally and vertically along the fractures, forming quartz veins and tension fractures under different temperature conditions. Moreover, changes in salinity, pressure, and carbon dioxide of deep fluids, varying from acidic to weakly alkaline, resulted in earlier calcite precipitation in contraction fractures and weathered fractures. Tectonic uplift resulted in the long-term exposure of volcanic rocks, where fresh water mixed with the partially alkaline fluid escaping the basin to form calcite cements, thus retaining the characteristics of a seepage environment in the weathered fractures. Structural fractures occurred due to tectonic movements during the burial period. Filling and leakage of hydrocarbons caused pore fluids to convert from acidic to alkaline, precipitating late sparry calcite in dissolution fractures. Late hydrothermal fluid metasomatism, brought about by infiltration into the permeable zone, caused partial dissolution of local calcite along cleavage cracks.

Keywords: fracture fillings; alteration haloes; volcanic rock; fluid activity; Junggar Basin

1. Introduction

Volcanic rock reservoirs have been described in many locations around the world (e.g., Scott Reef Gas Field of the Browse Basin in Australia, the Jatibarang Oil Field of Northwest Java Basin in Indonesia, and the Yoshii-Kashiwazaki Gas Field in the Niigata Basin in Japan) [1,2]. The reservoir rocks range from basalt to andesite or rhyolite formed during various geological times [3]. As a new direction in hydrocarbon exploration, volcanic reservoirs are attracting the attention and interest of scholars in the oil industry [4]. In the last few years, a significant number of volcanic hydrocarbon reservoirs have been reported in western China [5–10]. In particular, a breakthrough was achieved in volcanic rock exploration in the Carboniferous of the Junggar Basin when the Kelameili Gas Field was discovered, offering good prospects for exploration in the Kelameili area.

The reservoirs types are interpreted to be fracture-controlled, and intensively altered by diagenetic processes. In addition, fracture-pore reservoirs are thought to be primary types of Carboniferous volcanic reservoirs in the Kelameili Gas Field [11]. Previous studies suggested that volcanism, diagenesis, tectonic stress, and seeping water/organic acids caused the occurrence of fractures in the volcanic rocks [12]. Most workers who accept the fracture system as the key factor in controlling hydrocarbon accumulation, and crucial for volcanic rocks reservoirs, agree that the fractures are partial reservoir spaces linked with seepage pathways, and most commonly associated with fluid infiltration [13]. This is based on the characteristics of fractures as interpreted from petrographic studies and from geochemical data [14–17].

The degree of filling of the fractures is also an important signature used to evaluate whether volcanic reservoirs have developed. After the multi-stage dissolution of volcanic rocks by acid fluids, corresponding carbonates and other minerals were precipitated [18]. Furthermore, changes in the carbon dioxide content, salinity, temperature, and pressure of deep fluids also affect dissolution-filling processes [9,19]. The filling processes of minerals in fractures are commonly overlooked as a possible critical element for investigating the formation mechanisms of volcanic reservoirs. However, previous research has mostly focused on the characteristics of volcanic reservoirs and hydrocarbon accumulation in the Junggar Basin. This article is mainly concentrated on the Carboniferous Batamayineishan Formation in the Dixi Area, Junggar Basin, Northwestern China, which has recently become of special interest for gas exploration of volcanic reservoirs.

Our main objectives are: (1) to address the petrographic and geochemical data from cores and geochemical results; (2) to describe the fracture fillings in the volcanic reservoirs; and (3) to investigate the origin of the fluid activities. In this way, the Carboniferous volcanic reservoirs may serve as a new direction for research into the formation mechanisms of similar volcanic reservoirs.

2. Geological Setting

The Dixi Area is located in the central and western region of the Luliang Uplift of the Junggar Basin. The study area is located between the Western Dishuiquan Fault and the Northern Dishuiquan Fault (Figure 1). In the Late Carboniferous, the basin became a closed inland basin. Deep crustal melting and magmatic activity were induced by intense continental collisions, and formed volcanic-sedimentary rocks linked to explosive activity facies, volcanic lavas of overflow facies, subvolcanic rocks, and minor volcanic sedimentary rocks [20–22]. The Carboniferous succession is subdivided into the Lower Carboniferous Tamugang Formation, the Dishuiquan Formation and the Upper Carboniferous Batamayineishan Formation. The Batamayineishan Formation volcanic rocks are the products of the mixing of crust and mantle magmas. The magma sources are inferred to be mainly composed of depleted mantle material that formed during southward subduction of the PaleoAsian Ocean in the Late Palaeozoic [23].

The thickness of the Batamayineishan Formation in the Dixi Area is up to 1700 m, with a burial depth of 2200–3600 m, and represents a depositional sequence formed by volcanic activity and sea-level fluctuation. Three eruptive-sedimentary cycles separate the Batamayineishan Formation into the lower First Member (C_2b_1), middle Second Member (C_2b_2), and upper Third Member (C_2b_3). The volcanic activity weakened gradually in each cycle, forming several successions of volcanic rocks near the base and volcano-sedimentary rocks near the top (Figure 2). The accumulation of hydrocarbons is mainly controlled by the source rocks of the Lower Carboniferous Dishuiquan Formation and caprocks of the Upper Carboniferous Wutonggou Formation [24]. Thus, structural-stratigraphic hydrocarbon reservoirs and lithologic reservoirs are developed at the top of Batamayineishan Formation in the Dixi Area (Figure 3). Uplift and denudation in the latest Carboniferous were caused by tectonic collision. As a result, a weathered crust reservoir of volcanic rocks in a paleo-high with slope zones were formed by weathering dissolution. In addition to the weathering, the influx of deep fluid can also not be ignored. Subsequently, deep fluids migrated upwards mainly through faults and reacted with the surrounding rocks. Ore-forming materials derived from deep fluids precipitated in the fissures of surrounding rocks, and had an intense influence in the igneous reservoirs [25].

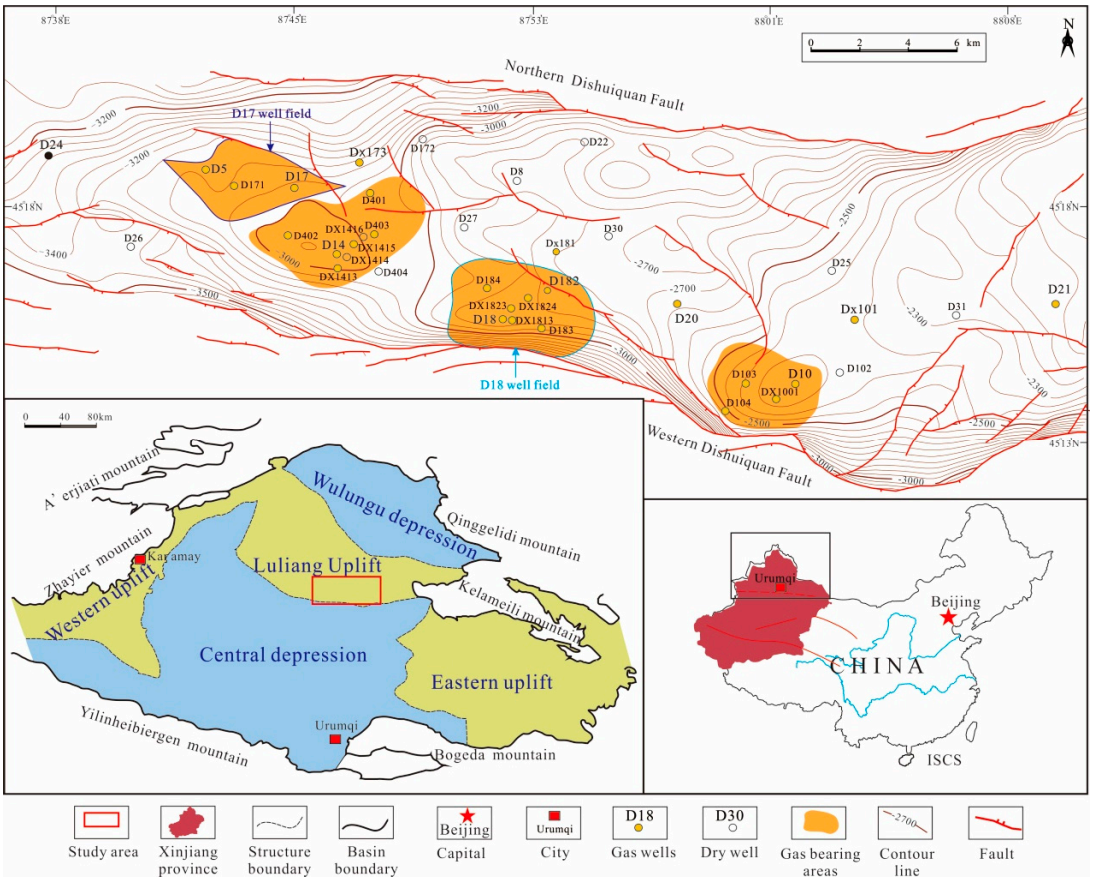

Figure 1. Structural location map of Dixi Area in Kelameili Gas Field, Junggar Basin.

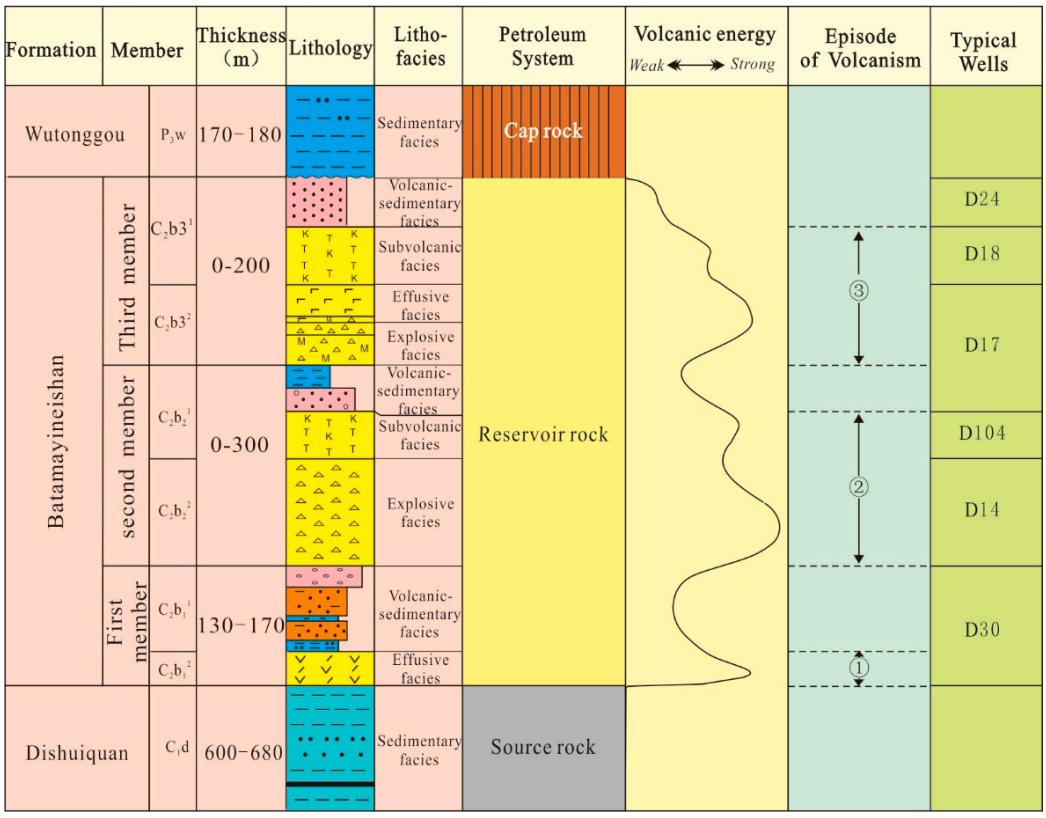

Figure 2. Simplified stratum column of Dixi Area in Kelameili Gas Field, Junggar Basin.

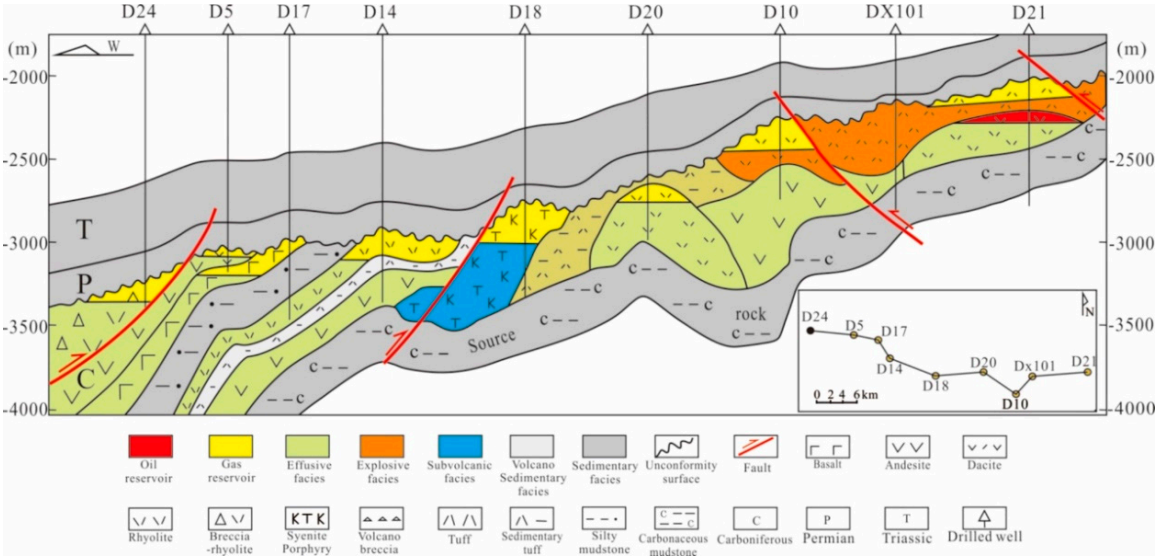

Figure 3. Hydrocarbon-reservoir section of Carboniferous volcanic rocks in the Dixi Area.

Mafic to acid igneous rocks are widely distributed in the Batamayineishan Formation. A petrochemical study suggests the volcanics are mainly of calc-alkaline series, with some weakly alkaline series according to the Rittmann Serial Index (σ) calculation [26]. The rocks are mainly composed of basalt, although the intermediate volcanic rocks are mostly composed of trachyte, followed by andesite or andesitic breccia (tuff), while the acidic volcanic rocks are composed mainly of rhyolitic tuff. The weakly alkaline volcanic rocks are mainly developed in subvolcanic facies distribution zones in the D18 field well (Figure 3), and are mainly composed of trachyte, syenite and monzonite porphyritic rocks.

3. Samples and Methods

The calcite cements in the fractures were studied by optical and cold cathodoluminescence (CL) petrography. Polished slabs and thin sections were stained with Alizarin Red S and potassium ferricyanide. CL petrography was carried out with a Technosyn Cold Cathodoluminescence Model 8200 MkII (CL 8200 MK5, Cambridge Image Technology LTD., Cambridge, UK). The elemental compositions of the calcite, quartz veins, and diagnostic minerals were quantitatively analyzed by Electron Probe Micro Analysis (EPMA) (ZEISS EV0 MA15, Carl Zeiss Microscopic Image Company Ltd., Oberkochen, Germany) combined with X-ray Diffraction (XRD) (X Pert PRO MPD, Panaco Netherlands, Almelo, The Netherlands). The EPMA was done under an accelerating voltage of 20 kV and a beam current of 600 mA.

Eleven stable isotopic analyses were carried out at the Southwest Petroleum University using the carbonate reaction method. Samples were connected using a micro-drilling method to avoid contamination, after handpicking to attain a purity of >99%, the minerals were pulverized to less than 150 μm, then the samples were reacted by the application of the phosphoric acid bath method at 90 °C, and the CO_2 generated was examined through use of Elementar IsoPrime MAT253 mass spectrometer (Isoprime100, Isoprime, Germany). Oxygen and carbon isotope data were converted to permil (‰) relative to Vienna Pee Dee Belemnite (V-PDB), and were corrected by fractionation factors supplied by Fairchild and Spiro [27]. Precision of the δ18O and δ13C ratios data was better than ±0.1‰.

Analysis of fluid inclusion types and occurrences were carried out using Leica DM2500P fluorescence microscope (DM 2500P, Yizhi Instruments Company Ltd., Wuhan, China) in the State Key Laboratory of the Southwest Petroleum University. Ultra-violet fluorescence was carried out on the same microscope. Temperatures of homogenisation were determined using a Linkam THMS 600 microscope (THMS 600, LINKAM Scientific Instruments, Tadworth, UK) with heating/freezing

system. The analytical error was small (±1 °C) compared to the range of the results. The vapor and liquid components of single fluid inclusions were determined by Almega XR laser Raman spectrometer (Nicolet Almega XR, Thermo Fisher Scientific, Waltham, MA, USA). High-resolution imaging and semi-quantitative X-ray microanalysis were carried out using Quanta FEG650 scanning electron microscope (Quanta 650, FEI, Hillsboro, OR, USA) in the State Key Laboratory of the Southwest Petroleum University.

4. Fracture Characterization

Fractured reservoirs are the main reservoir type and the key to forming effective reservoirs in the Dixi Area. The igneous rock fractures are mainly oblique, crossing fractures (~50%), followed by reticular ones (~28%), with a few orthogonal ones (~12%). In the D18 field well, subvolcanic rocks have the most developed fractures, with fracture segments accounting for more than 70% of the total thickness, followed by basalt and andesitic basalt in the D17 well area (~50%), while acid rhyolite, volcaniclastic rocks, volcaniclastic sedimentary rocks have fewer fractures. Fractures are controlled by faults and structural position. Fractures in well D18 and well D182 are near the Western Dishuiquan Fault and are structurally relatively high and the most developed, while those in well Dx181 and well Dx173 lie far from the fault, are in a structurally relatively low position, and are the least developed.

Based on surface morphology, geometry, infilling [28,29] and other classification criteria [30], the fractures of the igneous reservoirs are divided into primary fractures and secondary fractures. The primary fractures include explosion fractures (EF), contraction fractures (CF), and vertical tension fractures (VTF). The secondary fractures include weathered fractures (WF), oblique crossing structural fractures (OCSF), shear structural fractures (SSF), and dissolution fractures (DF). Primary fractures were mainly formed by explosion of water and volatiles below a crystalline rind, or contraction by cooling of crystallized magma, or upwelling forces of magma from the depth. Secondary fractures were formed by weathering, regional stress or dissolution by various fluids. Fractures of various mechanisms together can lead to irregular reticular fractures, and the fractures are mainly filled with calcite and quartz, with clear cross-cutting relationships (Figure 4). The occurrence, pore-filling minerals, and geochemical data for the different types of fractures are significantly different (Table 1).

4.1. Explosion Fractures

These irregular-shaped fractures cut rocks into breccia like pieces with no significant displacement, forming breccia-like rocks (Figure 4A). These fractures are mainly filled with quartz (Figure 4G) and mostly occur in the top of hypabyssal or ultra-hypabyssal intrusive bodies, suggesting that the fractures are mainly formed by Deep magma upwelling destroys upper lava or magma crypto-explosion activity [31]. Deep magma moved up and mixed with surrounding rocks, leading to condensation, crystallization and solidification, and formation of condensed shells. Decreased pressure led to various volatile components in the magma escaping from lower down and accumulating in the condensed shells at the top of intrusive bodies. When the accumulation reached a critical level, a violent explosion occurred and the condensed shells were broken, forming fractures.

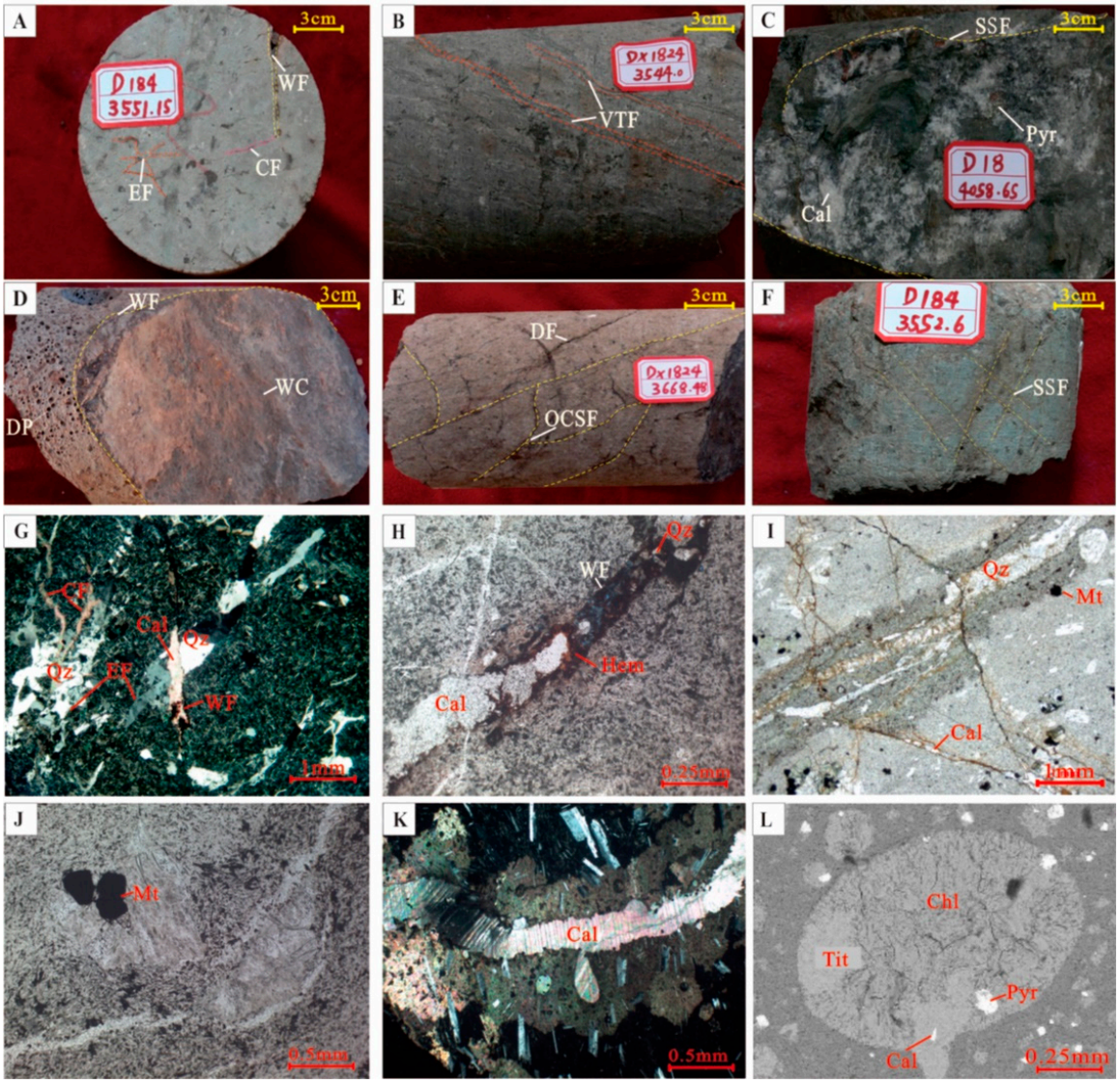

Figure 4. Macro photographs and photomicrographs of fracture fillings and alteration haloes from the Carboniferous Batamayineishan Formation, Dixi Area. (**A**) Multiple genetic fractures (WF, CF, EF) in andesite superimposed into irregular net, core picture; (**B**) vertical tension fractures (VTF) in andesite are completely filled with quartz, color on both sides of fissure is clearly darker than the surrounding rock, core picture; (**C**) fractures (SSF) of volcanic breccia filled with calcite and idiomorphic granular pyrite, core picture; (**D**) weathered fractures of orthophyre filled with red weathered clay (WC), dissolution pores (DP) are developed, core picture; (**E**) Oblique crossing structural fracture (OCSF) and dissolution fracture (DF) of orthophyre, core picture; (**F**) shear structural fracture (SSF) in andesite are completely filled with calcite, core picture; (**G**) fractures in veins and branches cutting the rock into brecciated structure; time of formation of quartz vein is earlier than that of calcite vein, (+); (**H**) weathered fractures filled with red weathered clay, vadose silt and sparry calcite, (+); (**I**) quartz vein formed due to activity of hydrothermal fluid is cut by later structural fractures, which are filled with calcite, (−); (**J**) fractures bypass phenocryst, Ti-bearing magnetite (Mt) with relatively good degree of idiomorphism is seen in the surrounding rock to the fracture, (−); (**K**) fractures filled with calcite; two sides of alteration haloes along the fractures are distributed with matrix minerals and pore voids, (+); (**L**) pores filled with chlorite, sphene and pyrite, (backscattered electron image). Cal = calcite; Pyr = pyrite; Qz = quartz; Hem = hematite; Mt = ilmenite; Tit = titanite; Chl = chlorite; (−) = plane polarized light; + = cross polarized light.

Table 1. Classification and filling characteristics of volcanic fractures in the Dixi Area.

Classification		Characteristics and Indictors	Infilling and Luminescent under Cathode Luminescence (CL)	Position	Mechanism
Primary fractures	EF	Multiple directions, uneven fracture widths, irregular radial patterns from centers, and matching adjacent boundaries	Quartz (non-luminous), no alteration halo	Near to the shattered zone	Deep magma upwelling destroys upper lava, or cryptoexplosion
	CF	Extremely irregular shapes, reticular, concentric, horsetail-shaped, broom-shaped or cracked	Calcite (orange light), without Fe, no alteration halo	Widely distributed in different occurrence throughout rock	Contraction by cooling of crystallized magma
	VTF	A series of steeply dipping and near-vertical fractures of varying widths and matching serrated walls, bypassing phenocrysts	Quartz (purplish red), contain Ti, Mn, alteration halo	Great thickness, near to magma channel	Upwelling forces of magma from the depth
Secondary fractures	WF	No-direction; horsetail-shaped, echelon, leaf vein type	Calcite (reddish orange light), hematite	Upper part of rock masses	Weathering
	OCSF	Nearly vertical, dip angle exceeding 75°, uneven fracture surface, cutting through rocks	Calcite (reddish orange light), without Fe, alteration halo	Lower part of rock masses	Regional stress
	SSF	Two groups of conjugated fractures, relatively flat fracture surface, cutting through particles	Calcite (dark red light), contain Fe, hydrocarbons	Near to faults	
	DF	Non-specific orientation, irregular fracture walls, connected with dissolution pores and cavities	Quartz, calcite, hydrocarbons	Along fractures and structural high	Dissolution by various fluids

EF, Explosion fracture; CF, Contraction fracture; VTF, Vertical tension fracture; WF, Weathered fracture; OCSF, Oblique crossing structural fracture; SSF, Shear structural fracture; DF, Dissolution fracture.

4.2. Contraction Fractures

These fractures are of extremely irregular shape with no obvious dissolution at the fissure walls, are mainly filled with calcite and cut through explosion fractures (Figure 4A,G). These fractures are widely distributed at the top, bottom, and sides of the rock mass. Contraction fractures are formed by cooling and shrinking of the rock mass after completely solidified.

4.3. Vertical Tension Fractures

These are a series of steep and near-vertical fractures. On the both sides of the surrounding rocks, a dark belt of about 2 mm wide is often developed (Figure 4B). The dark belt is characterized by increased particle sizes of chlorite and sericite and a large quantity of small and regular-shaped opaque minerals (Figures 4I and 5E). The fractures cut through phenocrysts and are filled with quartz. Quartz shows undulating extinction under a plane-polarized light microscope, and is bluish purple luminescent under CL (Figure 5B). Tension fractures are an effective indictor for the presence of abnormally high pressure in the paleo-fluids in sedimentary basins [32]. Vertical tension fractures in volcanic rocks are considered to be formed by the force of upwelling magma from depth [33].

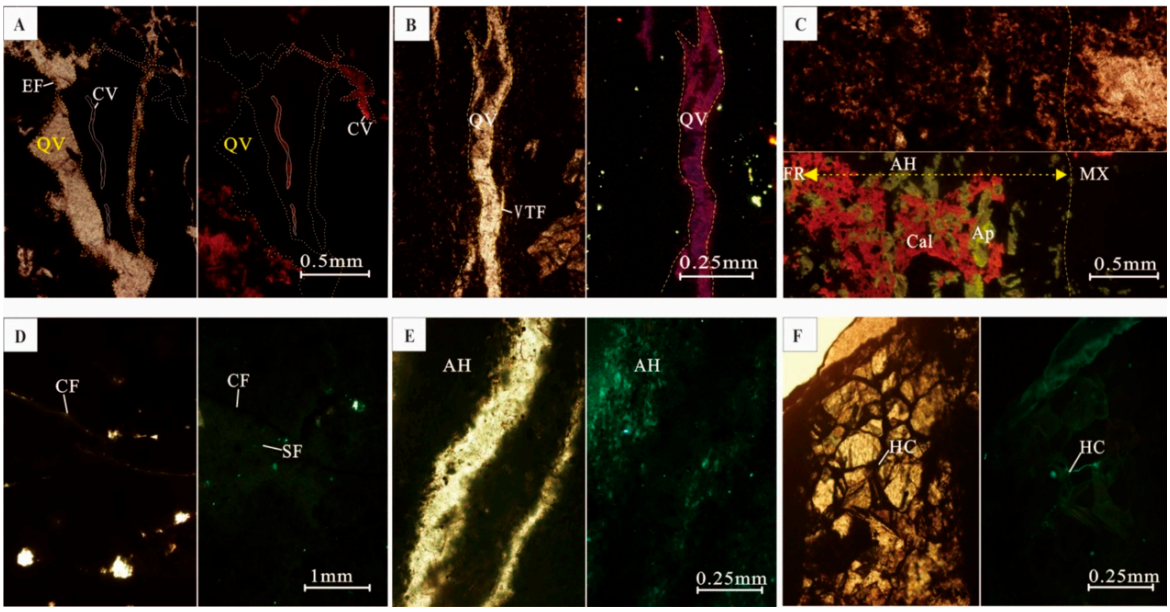

Figure 5. Photomicrographs of fracture fillings and alteration haloes under cathodoluminescence microscopy and ultraviolet light from the Carboniferous Batamayineishan Formation, Dixi Area. (**A**) Calcite vein (CV) filled in fractures emitting orange light under cathodoluminescence (CL) microscopy, quartz vein (QV) in explosion fractures not emitting, DX1824 well, 3637.48 m, plane-polarized light/CL; (**B**) quartz vein filled in the vertical tension fractures emitting purple-red light under cathodoluminescence microscopy, DX1824 well, 3548.3 m, plane-polarized light/CL; (**C**) calcite emitting orange light, metasomatic matrix (MX) minerals, apatite (Ap) emitting yellow light can be seen in the calcite, D18 well, 4058.55 m, plane-polarized light/CL; (**D**) contraction fractures are dislocated by structural fracture, structural fracture (SF) emitting blue fluorescence, but not in contraction fracture, DX1824 well, 3637.48 m, plane-polarized light/ultraviolet light; (**E**) micro pores abundant in alteration haloes on both sides of cracks, emit blue fluorescence, DX1824 well, 3548.3 m, plane-polarized light/ultraviolet light; (**F**) hydrocarbons occur along calcite grains boundary, emit blue-white light, presenting a relatively high maturity, D18 well, 4058.55 m, plane-polarized light/ultraviolet light. CF = contraction fracture; EF = explosion fracture; SF = structural fracture; VTF = vertical tension fracture; WF = weathered fracture. AH = alteration halo; Ap = apatite; Cal = calcite; HC = hydrocarbon; MX = matrix.

4.4. Weathered Fractures

These fractures do not possess a specific orientation with very irregular shapes, and are mainly filled with sparry calcite (Figure 4A), vadose silt, and red clay mineral (hematite) with clear boundaries (Figure 4A,D,H). Insoluble limonite occurring along the fractures is formed by supergene leaching, and is partly altered by hematisation due to dehydration [34,35]. Calcites are reddish orange luminescent under cathode luminescence (CL), and are darker luminescent under CL at the edges of fractures when in the presence of hematite (Figure 5A).

4.5. Oblique Crossing Structural Fractures

Nearly vertical fractures with dip angles exceeding 75°, and uneven fracture surfaces. The fractures cut through the rocks and are mainly filled with sparry calcite, and have alteration haloes 0.5–1 mm in width on both sides of the fissure (Figure 4E,K). The alteration haloes are characterized by a large amount of fine-grained euhedral pyrite framboids. Residual chlorites are distributed in the surrounding pores that have not been completely replaced (Figure 4L), suggesting that the metasomatism of the sparry calcite occurred significantly later than the chlorite filling. The calcite veins are commonly filled by idiomorphic-granular opaque minerals such as pyrite, and rarely sphalerite (Figure 5C). Calcites are orange luminescent under CL, and the interspersed idiomorphic apatites are yellow luminescent (Figure 5F). Early structural fractures are mainly found in the lower parts of the igneous strata, as a result of post-intrusion regional stress.

4.6. Shear Structural Fractures

These consist of two groups of conjugated fractures, with one group having a high dip angle and the other group having a lower dip angle. The fractures cut through particles and phenocrysts (Figure 4C,F,D), with relative straightness and small variation of fracture width. Structural fractures are mainly found near faults, and their occurrence and scale are proportional with the direction of the tectonic stress field and the intensity of tectonic stress. Various scales of late structural fractures are developed, varying from both extensive faults (at a scale of hundreds of meters) that cut through the entire volcanic rock mass to millimetre-scale micro-fractures.

4.7. Dissolution Fractures

Dissolution fractures are primary fractures formed at the early diagenetic stage or tectonic fractures caused by late tectonic stresses, but that underwent late hydrothermal processes or dissolution [36]. The shape and distribution of the primary fractures can be distinguished though the dissolution fractures have been dissolved, while the primary fractures cannot be identified because of the further development of the dissolution fractures. In the Dixi area, the morphology of dissolution fracture is enlarged and changed after the corrosion dissolved by various fluid (Figure 4E). Dissolution fractures have irregular surfaces and often connect with dissolution vugs. The fracture-fillings are complex, including filled, half-filled and unfilled fractures. Residual hydrocarbons are commonly observed at the sides of the fractures, which were later filled by calcite (Figure 5E,F).

5. Results

Thirty-seven samples of cores from six wells were analyzed for petrography and geochemistry.

In the quartz fillings of the vertical tension fractures, about 0.02 wt % TiO_2 and 0.02 wt % MnO were detected. The opaque mineral in the alteration haloes on both sides of the quartz veins was confirmed to be magnetite, with TiO_2 contents of between 0.5 wt % and 3 wt % (Table 2). In some unaltered rocks, the TiO_2 contents may reach 10 wt %, while MnO was also detected. The homogenization temperatures measured from the brine inclusions in quartz (Figure 6A) veins range from 96 to 111 °C, with an average of 104.79 °C.

Table 2. Electron probe-spectroscopy data of secondary minerals of the Carboniferous igneous rocks in the Dixi Area.

Well Name	Sample ID	Depth	SiO_2	CaO	TiO_2	FeO	Fe_2O_3	MnO	Fe	F	S	P_2O_5	CO_2	C	Unit	Mineral
		(m)	(%)	(%)	(%)	(%)	(%)	(%)	(%)	(%)	(%)	(%)	(%)	(%)		
DX1824	DX1824-1	3548.30	99.97	-	0.02	0.004	-	0.004	-	-	-	-	-	-	wt %	quartz
DX1824	DX1824-2	3548.30	99.97	-	-	0.006	-	0.021	-	-	-	-	-	-	wt %	quartz
DX1824	DX1824-3	3548.30	-	42.42	-	-	-	-	-	5.42	-	43.13	-	9.03	wt %	apatite
DX1824	DX1824-5	3637.00	-	-	43.40	15.73	17.47	23.40	-	-	-	-	-	-	wt %	ilmenite
DX1824	DX1824-6	3548.30	-	-	0.53	28.88	70.59	-	-	-	-	-	-	-	wt %	magnetite
DX1824	DX1824-7	3548.30	-	-	3.06	28.15	68.79	-	-	-	-	-	-	-	wt %	magnetite
D18	D18-1	4058.55	-	-	-	-	-	-	44.61	-	55.39	-	-	-	wt %	pyrite
D18	D18-2	4058.55	-	-	-	-	-	-	44.13	-	55.87	-	-	-	wt %	pyrite
D18	D18-4	4058.55	-	38.62	-	-	-	-	-	6.45	-	41.72	-	13.21	wt %	apatite
DX1824	DX1824-4	3637.00	-	34.61	-	1.76	-	-	-	-	-	-	63.63	-	at %	calcite
D18	D18-3	4058.55	-	31.30	-	-	-	-	-	-	-	-	68.70	-	at %	calcite

All data are normalized to 100. - indicates no available data.

The EPMA results showed that fracture-filled calcites are mainly non-ferroan calcite, but are partly ferro-calcite containing small amounts of FeO (1.76 at %). The opaque mineral in the calcite veins was confirmed to be pure pyrite. In addition, apatite associated with calcite and pyrite is mainly carbonate-fluorapatite. The homogenization temperatures measured from the brine inclusions in calcite veins (Figure 6B–D) range from 96.5 to 115 °C, with an average of 104.99 °C (Table 3, Figure 6E). The results of laser Raman spectrometric analysis indicate that the main compositional components of the liquid in the fluid inclusions are bicarbonate, carbanion and water, while their vapor is mainly composed of carbon dioxide, methane, and water.

The bulk isotopic compositions of calcite in tectonically-related fractures show $\delta^{18}O$ values of between −21.5‰ and −14.4‰, with an average of −18.2‰, while $\delta^{13}C$ values range between −21.06‰ and −11.01‰, with an average of −15.96‰ (Table 4). The $\delta^{18}O$ (PDB) compositions of calcite in weathered fractures, on the other hand, were measured between −16.1‰ and −11.06‰, with an average of −13.3‰, and $\delta^{13}C$ values were between −15.57‰ and −11.01‰, with an average of −12.76‰.

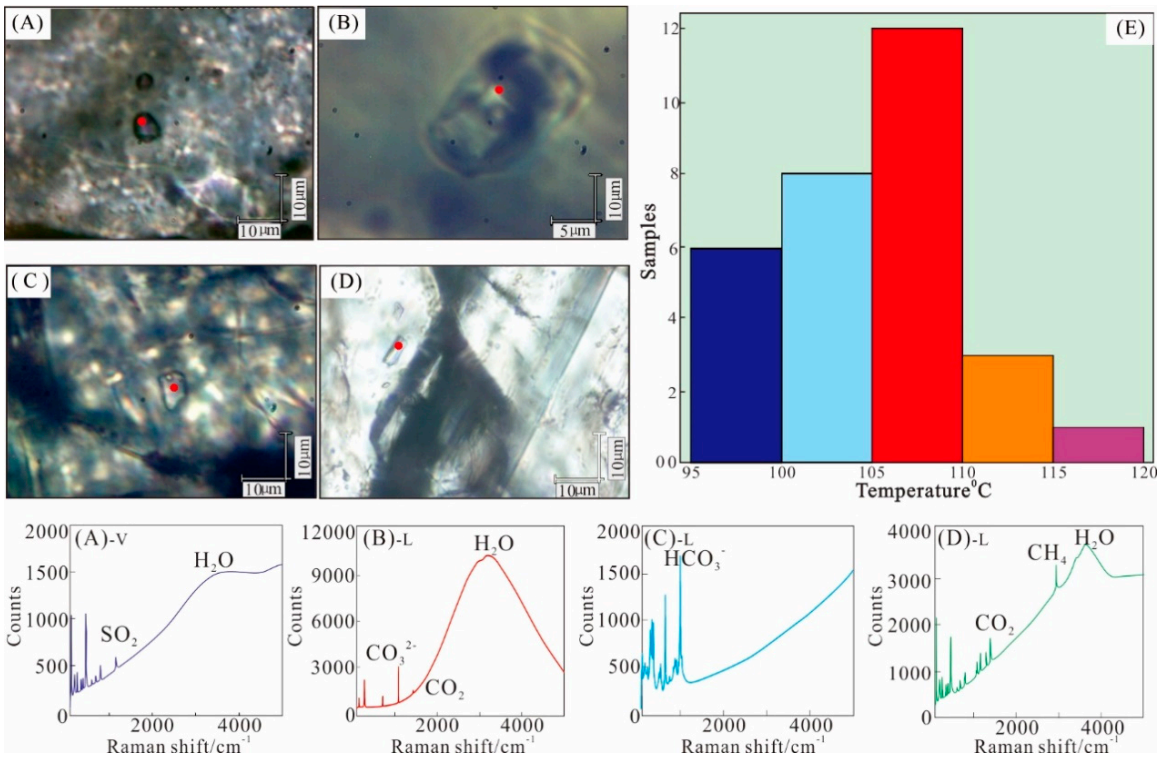

Figure 6. Inclusions and Laser Raman spectrum characteristics of contained in quartz veins (**A**) and calcite veins (**B**–**D**) and frequency histogram of fluid inclusion homogenization temperature (**E**). Abscissa is Raman shift in the unit of cm^{-1}, and ordinate is Raman scattering relative strength in the unit of count/second (L, liquid phase; V, gas phase).

Table 3. Fluid inclusion homogenization temperature (Th) of the Carboniferous igneous reservoirs in the Dixi Area.

Well Name	Sample ID	Depth (m)	Lithology	Size (μm)	Vapor Liquid Ratio (%)	Position	FI Type	Th aq (°C)
D18	46-1	4058.55	basaltic andesite	7	10	calcite	pr	113, 115, 118.5 (3)
D18	46-2	4058.55	basaltic andesite	6	5	calcite	pr	102.5, 105.6 (2)
D18	46-4	4058.55	basaltic andesite	8	5~10	calcite	pr	108, 108.8, 109 (3)
D18	46-7	4058.55	basaltic andesite	6	5	calcite	pr/psec	99, 99, 101 (3)
D18	46-10	4058.55	basaltic andesite	6	5~10	calcite	pr	105.2, 106.8 (2)
DX1824	10-1	3637.48	Syenite porphyry	20	5~10	quartz	pr	104 (1)
DX1824	10-2	3637.48	Syenite porphyry	10	5~10	quartz	pr	106.6, 111 (2)
DX1824	10-4	3637.48	Syenite porphyry	5~10	5	quartz	psec	99.8, 103.9 (2)
DX1824	10-6	3637.48	Syenite porphyry	5	5	calcite	pr	107 (1)
DX1813	23-1	3465.5	Syenite porphyry	8	5~10	quartz	psec	96 (1)
DX1813	23-2	3465.5	Syenite porphyry	8	5~10	quartz	psec	107, 109.6 (2)
DX1813	23-3	3465.5	Syenite porphyry	5	5	quartz	sec	104, 106 (2)
DX1414	48-1	3722	sedimentary tuff	8	5~10	calcite	pr	103.5, 106.8 (2)
D184	49-1	3647.5	Syenite porphyry	10	5~10	calcite	pr	101, 103.5 (2)
D17	40-1	3642.5	Amygdaloidal basalt	15	5~10	calcite	pr	96.5, 98 (2)

Pr, primary; sec, secondary; psec, primary/secondary.

Table 4. Carbon, oxygen, and strontium isotopic compositions of calcite veins in the hosted Carboniferous igneous reservoirs in the Dixi Area.

Well Name	Sample ID	Depth (m)	Lithology	Occurrence	Detection Result			$^{87}Sr/^{86}Sr$
					$\delta^{13}C_{V\text{-}PDB}$ (‰)	$\delta^{18}O_{V\text{-}PDB}$ (‰)	$\delta^{18}O_{V\text{-}SMOW}$ (‰)	
DX1824	DX1824-1	3533.50	Gray-green trachyte	Weathering fracture	−11.7	−16.1	14.3	0.70461
DX1824	DX1824-2	3534.00	Gray-green trachyte	Contraction fracture	−14.6	−21.5	8.7	0.70458
DX1824	DX1824-3	3534.00	Gray-green trachyte	Weathering fracture	−15.57	−12.64	17.87	-
DX1824	DX1824-4	3537.00	Trachytic Tectonic breccia	Inter-breccia fracture	−18.1	−17.6	12.7	0.70337
DX1824	DX1824-5	3537.50	Trachytic Tectonic breccia	Inter-breccia fracture	−18.8	−20.5	9.7	0.7034
DX1824	DX1824-6	3548.30	Gray-green trachyte	Structural fracture	−15.3	−14.4	16	-
DX1824	DX1824-7	3637.48	Syenite porphyry	Weathering fracture	−11.01	−11.06	19.5	0.70431
DX1414	DX1414-1	3630.17	Vitric-Crystal tuff	Contraction fracture	−11.2	−17.3	13.1	0.70433
DX1414	DX1414-2	3722.00	sedimentary tuff	Structural fracture	−16.6	−17.1	13.3	0.70399
DX1414	DX1414-3	3722.00	sedimentary tuff	Structural fracture	−21.06	−19.65	10.64	0.70456
D18	D18-1	4058.55	Gray-green basaltic andesite	Structural fracture	−17	−17.8	12.5	0.70489

- indicates no available data.

6. Discussions

6.1. Trace Elements and Source of Fluid

Previous research has documented that the euhedral Mn-bearing, titanian magnetites are the products of late magmatism to the post-magmatic hydrothermal stage [37]. In the presence of the hydrothermal fluids moving along the fractures, the alteration haloes (i.e., dark belts) occur as the result of: (1) Fe, Mn, Ti, and other elements produced by the decomposition of minerals, such as Ti-bearing magnetite and chlorite, migrating to the hydrothermal veins; and (2) Ca in hydrothermal veins migrating and accumulating in host rocks during the alteration and waning stages.

Quartz filling in the vertical tension fractures is caused by condensation at high temperatures and by enrichment of high Ti contents in the crystal lattices (Table 2). This process also led to pyrite precipitation on both sides of the fractures in a reaction of Fe with S-bearing components in the hydrothermal fluids (Figure 4C). Quartz veins containing TiO_2 (Figure 4J) and MgO, and are bluish purple luminescent under CL, and alteration haloes containing pyrite in either side wall both indicate that the formation and filling of the vertical tension fractures are related to post-magmatic hydrothermal processes. Furthermore, the elevated temperature and fluid interactions are required to induce recrystallization of chlorite, sericite, and other clay minerals in the host rocks, resulting in increased mineral particle sizes and the development of intergranular mineral pores. The intergrowth texture of sparry calcite, apatite, pyrite, and other minerals in the igneous rock fractures suggest that they have a genetic relationship (Figures 4L and 5C).

Alkali feldspar is the main host mineral for phosphorus in peraluminous magma. In the hydrothermal stage, structural phosphorus released from feldspar crystals in the Al-Si ordering process can react with Ca^{2+} ions carried by the fluids to produce secondary apatite [38]. Previous researches indicated that the kinetics of carbanion entering the apatite crystal lattice are closely related to the HPO_4^{2-}/HCO^{3-} ratio and pH value. Higher ratios of $HPO4^{2-}/HCO^{3-}$ and elevated pH values are favorable for the carbanion to enter into the apatite crystal lattice [39]. The results also revealed that the phosphate mineral precipitated earlier than the carbonate minerals, with the first deposit being single carbonate-fluorapatite (CFA), followed by coexisting minerals of CFA and calcite, after which calcite significantly increased [40]. Similarly, calcium phosphate is often found associated with pyrite in the Dixi Area (Table 2). Both the gas and liquid composition of inclusions in the calcite contain carbon dioxide, implying that the precipitation of calcite was closely related to carbon dioxide and occurred in a reducing environment (Figure 6B,D). Moreover, the abundant pyrite associated with apatite and calcite in the wells of DX18 and DX1824 indicates the formation of the fluorapatite is more probably related to the replacement of carbonate minerals by deep hydrothermal fluids (Table 2), and the euhedral pyrite in the side walls of the fractures are probably the by-product of this process (Figure 4C).

6.2. Stable Isotopic Compositions and Fluid Source of Veins

$\delta^{13}C$ values of calcite veins (11 samples) from the Batamayineishan Formation appear notably more negative than that of sedimentary carbonate (the $\delta^{13}C$ values of the sedimentary carbonate minerals are close to 0.0‰) [41,42], and are different from that of the magmatic minerals, which have $\delta^{13}C$ values between −5.3‰ and −7.0‰, and that of minerals derived from organic matter, which have $\delta^{13}C$ values between −24‰ and −29‰ [43,44], indicating that the calcites originated from carbonate related to organic matter. The data indicate that carbon dioxide produced by thermocatalysis of organic matter mixed with Ca ions and led to calcite precipitation in the manner of fracture filling. Carbon dioxide and methane detected by laser Raman spectrometers from the composition of the liquid in fluid inclusions in calcite indicates that the formation of calcite veins is related to organic carbon genesis (Figure 6). Different occurrences of calcite show little difference in isotopic compositions (Figure 7), although the $\delta^{13}C$ values of calcite associated with hematite at the sides of weathering fractures are significantly more positive than that of the other types of calcite (Table 4), implying that the calcite was mixed by meteoric water.

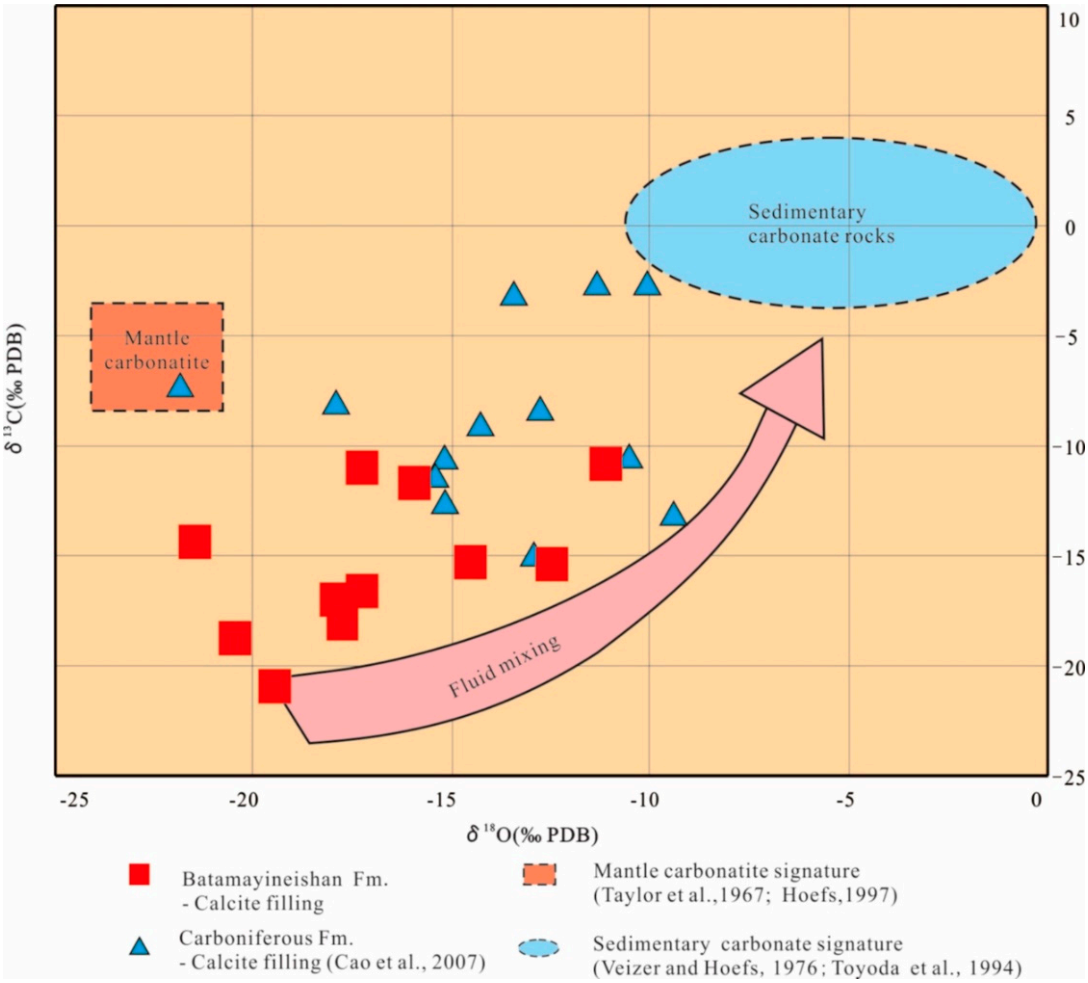

Figure 7. Carbon and oxygen isotope distributions of calcite veins in the study area.

Most of the calcite samples have negative $\delta^{13}C$ and $\delta^{18}O$ values, and there is a certain positive correlation between the $\delta^{13}C$ and $\delta^{18}O$ values, suggesting that the calcite was formed at relatively high temperatures during the late diagenetic stage [45,46]. The carbon and oxygen isotopic data for calcite falls mainly into the transitional zone between primitive mantle carbonatite and sedimentary carbonate (Figure 7), which is confirmed by the result of fluid inclusion (the average homogenization temperatures are 104.89 °C) (Table 3). Furthermore, the euhedral pyrite that occurs on both sides of the calcite veins, indicates that the pyrite precipitated before the calcite, as the product of deep hydrothermal metasomatic calcite in the post diagenetic stage.

The $^{87}Sr/^{86}Sr$ ratio of calcite cements is affected by seawater and diagenetic fluid. Calcites derived from the mantle generally have lower $^{87}Sr/^{86}Sr$ ratios than those formed from seawater or crust [47]. The average value of $^{87}Sr/^{86}Sr$ ratios of mantle and crust calcites are 0.703500 and 0.711900, respectively, while the strontium isotope values for the igneous calcite veins in the Carboniferous range from 0.703367 to 0.704892, with an average value of 0.704227. It is believed that these ratios are not significantly associated with depths or locations around the surface of unconformities or faults, but are related to the deeper hydrothermal fluids. The precipitation of calcite was the result of various types of fluid mixing.

6.3. Timing of Vein Formation and Hydrocarbon Fluid Activity

Three periods of hydrocarbon charges were identified by integrating the homogenization temperatures of fluid inclusions within the thermal evolution history (Figure 8). The timing of

the first stage oil charge, second stage gas charge, and third stage hydrocarbon adjustment were in Late Indosinian, Middle Yanshanian, and from Middle Yanshanian to the present, respectively. The close genetic relationship between hydrocarbons and calcite can provide information for determining the timing of hydrocarbon and fluid migration. After hydrocarbons leaked due to changes in the surrounding environment, such as a decrease in temperature, water erosion and biodegradation, bitumen was formed [48,49]. In addition, the bitumen is mainly distributed at the sides of the fractures, and the contact area of the calcite grains which filled in fractures are bluish purple under ultraviolet light, while the interior of calcite was not luminescent (Figure 5F), suggesting that the sparry calcite related with alteration halo may have formed after the early-stage hydrocarbon filling. Moreover, the timing of the occurrence can be pinpointed using a combination of evidence from both burial history and thermal history (Figure 8). Integrated burial history, strata temperature, temperature of fluid inclusion in minerals with the diagenetic event and tectonic movement, the time of various types of fracture fillings and hydrocarbon migration are pinpointed. The homogenisation temperature peak of calcite veins (100 to 115 °C) and the calculated results of the paleo-geothermal gradient of burial history suggest that formation time of the fluid inclusions was probably in the late Middle Jurassic. In summary, the SiO_2 components forming the quartz veins are primarily derived from the deep silica-rich hydrothermal fluids. The CO_2 sources forming the calcite veins are characterized by mixtures of hydrothermal fluid and deep hydrocarbon fluid. The dissolution of feldspar and transformation in clay minerals provide the major sources of Ca^{2+}, Fe^{3+}, and Mg^{2+} ions [50,51], and the basement faults and connected fractures are considered to serve as the migration pathways.

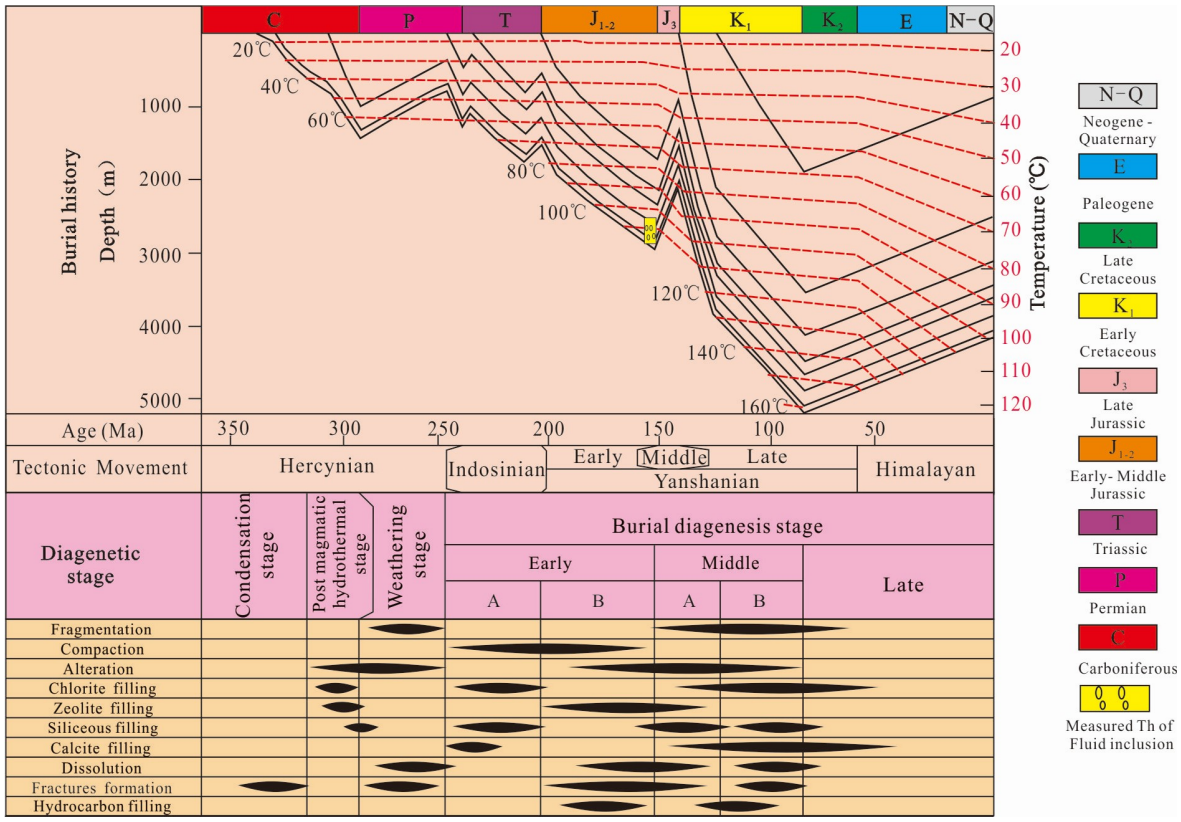

Figure 8. Burial-thermal history and diagenetic evolution of the Carboniferous Batamayineishan Formation for Dixi Area [48].

6.4. Paragenetic Model of Fracture Fillings

In Figure 9 the conceptual model for the generation and the evolution of the fractures in the volcanic reservoir of the Carboniferous Batamayineishan Formation of the Kelameili Gas Field are

presented (Figure 9). We can notice that the fracture-fillings are classified into 4 stages; (1) Stage I: high temperature quartz, (2) Stage II: low temperature quartz, (3) Stage III: early calcite, (4) Stage IV: bitumen and late calcite.

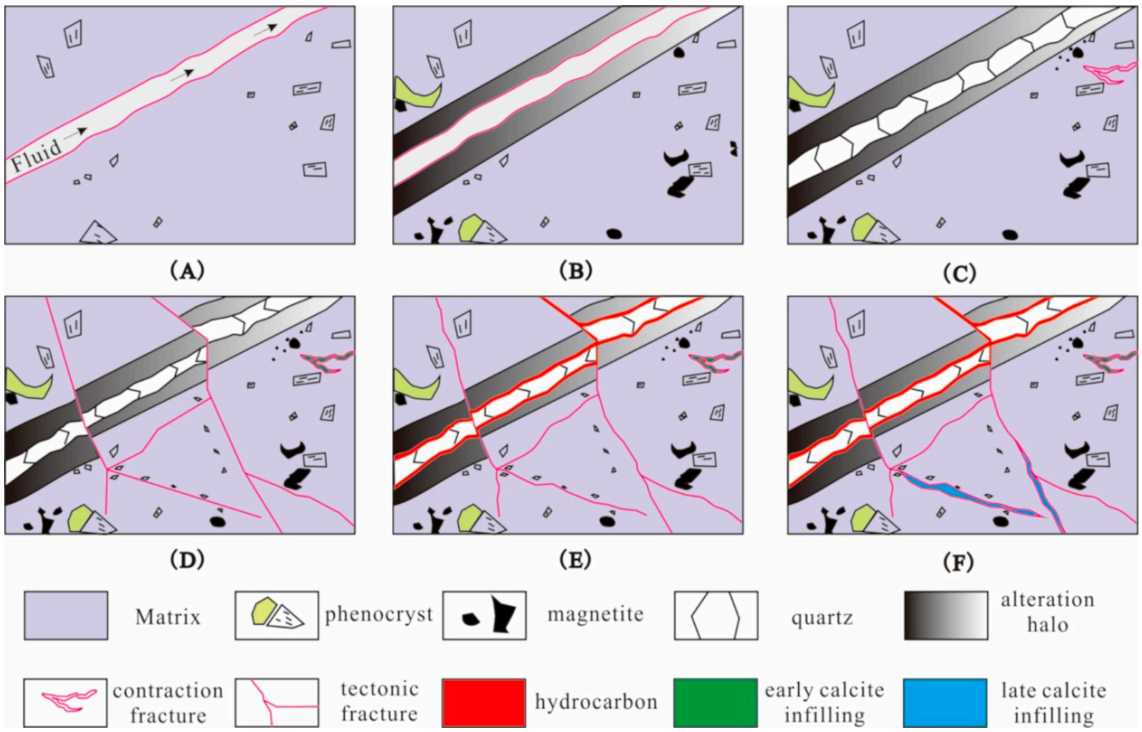

Figure 9. Conceptual model for fracture evolution of the volcanic rocks of the Carboniferous Batamayineishan Formation of the Kelameili Gas Field. (**A**) Hydrothermal fluids infilling; (**B**) migration of elements; (**C**) quartz veins and early calcite formed; (**D**) tectonic fractures formed; (**E**) hydrocarbon emplacement; (**F**) late calcite precipitation.

(1) Stage I: high temperature quartz

In the early stage, under the dual driving force of the pressure gradient and buoyancy, silica-bearing hydrothermal fluid moved upwards and along both sides of the fault, where vertical tension fissures were formed laterally, due to the rapidly decreased pressure, and alteration haloes were formed on both sides of the fissure. Reduced temperature lead to the precipitation of pyrite, and the quartz that filled in the fractures are bluish purple luminescent under CL (Figure 5B), which is probably formed at high temperatures and by high Ti contents in the crystal lattices [52,53].

(2) Stage II: low temperature quartz

The silica-bearing hydrothermal fluid in the process of moving upwards was trapped by overlying stratum, and gas accumulation or magma water interaction led to crypto-explosions, thereby forming explosion fractures characterized by their irregular radial shape from the centre outwards. Moreover, the decreases in temperature and pressure that accompanied the crypto-explosions are important factors causing low-temperature quartz veins to precipitate among the breccias, and the quartz that filled in the fractures were non-luminescent under CL (Figure 5A). The contraction and weathered fractures were formed when the rock mass condensed-contracted and weathered, respectively.

(3) Stage III: early calcite

The deep fluid gradually changed from acid to alkaline by the reaction with the surrounding rocks in the process of moving along faults and fractures. Furthermore, the reduction in the carbon dioxide contents and salinity, which resulted from a decrease of pressure and fluid mixing, led to early calcite precipitation in the contraction fractures. Under these particular conditions, the subsurface rocks undergo long-term exposure, when fresh water mixed with the partial alkaline fluid leaking out

of the basin, and formed calcite cements that retain the characteristics of the vadose environment in the weathered fractures.

(4) Stage IV: bitumen and late calcite

Residual bitumen persisted on the sides of structural fractures, which were earlier filled with hydrocarbons (Late Jurassic) and later leakage. Meanwhile, the pore fluid further changed from being acidic to alkaline, and the later calcite precipitated in the fissures (Figure 9).

Evidently, the fractures were converted from leakage to sealing due to infillings of quartz and calcite, which was mainly destructive to porosity and permeability of the reservoirs in study area. However, the altered rock strength had been decreased significantly, and these rocks were readily broken in the late tectonic movement and formed favorable hydrocarbon reservoirs [28]. As a result, many intergranular micro-pores were formed by the recrystallization of the clay mineral matrix and calcite in the alteration zones, which are conducive to the dissolution of minerals, assisted by late acidic fluids, forming a large number of secondary dissolved pores (Figure 4D), and becoming a significant hydrocarbon reservoir.

7. Conclusions

The study of the fractures of the Carboniferous Batamayineishan Formation of the Kelameili Gas Field led to the conceptual model of Figure 9, in which the genesis and the evolution stage of the different types of fracture fillings are presented. The results of this study can be schematized in the following points:

(1) Various types of fractures, which are commonly filled with quartz, and calcite, are developed in the Carboniferous igneous rocks of the Dixi Area. The formation of quartz is related to hydrothermal fluid derived from the basement. The occurrence of alteration haloes is the result of migration and convergence of elements when the alteration of the surrounding rock was waning. The sparry calcite is derived from carbonate related to deep hydrothermal fluids and organic matter, which were mainly formed in the terminal Jurassic.

(2) Silicic hydrothermal fluid enriched in volatile components escaped along faults, and filled quartz veins and tension fractures, which indicate high temperature and concealed explosive-low temperature conditions, respectively.

(3) Carbon dioxide and organic acids arising from volcanic magma activity were dissolved to form an acidic fluid, thereby accelerating the dissolution and albitization of the aluminosilicate minerals of the surrounding rock and the transformation of the clay minerals, and provided the foundation for the formation of carbonate minerals. Earlier calcite precipitation in contraction fractures and weathered fractures was caused by the decreasing salinity, pressure, and carbon dioxide content of deep fluids, varying from acidic to weakly alkaline. The filling and leakage of hydrocarbons in tectonic fractures in the Late Jurassic, caused the pore fluids to change from being acidic to alkaline, with the late sparry calcite precipitated in the dissolution apertures.

Author Contributions: Conceptualization, T.L. (Tian Liu), M.F., A.X., and X.L.; methodology, N.L., T.L. (Tong Lin); writing—original draft preparation, X.L., M.F.; writing—review and editing, M.F., T.L. (Tian Liu), X.L. and T.L. (Tong Lin); funding acquisition, X.L. and A.X.

Funding: This research was funded by the Key Project of the National Natural Science Foundation of China (Grant No. 4120219) and the Key Project of the National Natural Science Foundation of China (Grant No. 41502146).

Acknowledgments: Thanks are expressed to our colleagues involved in volcanic rocks researching in the Junggar Basin, as well as to a number of anonymous reviewers from which this article has benefited.

Conflicts of Interest: The authors declare no conflict of interest.

References

1. Schutter, S.R. Hydrocarbon occurence and exploration in and around igneous rocks. *Geol. Soc. Lond. Spec. Publ.* **2003**, *214*, 7–33. [CrossRef]

2. Lenhardt, N.; Götz, A.E. Volcanic settings and their reservoir potential: An outcrop analog study on the Miocene Tepoztlán Formation. Central Mexico. *J. Volcanol. Geotherm. Res.* **2011**, *204*, 66–75. [CrossRef]
3. Wang, P.J.; Chen, S.M. Cretaceous volcanic reservoirs and their exploration in the Songliao Basin, northeast China. *AAPG Bull.* **2015**, *99*, 499–523. [CrossRef]
4. Zou, C.N.; Zhao, W.Z.; Jia, C.Z.; Zhu, R.K.; Zhang, G.Y.; Zhao, X.; Yuan, X.J. Formation and distribution of volcanic hydrocarbon reservoirs in sedimentary basins of China. *Pet. Explor. Dev.* **2008**, *35*, 257–271. [CrossRef]
5. Wang, P.J.; Hou, Q.J.; Cheng, R.H.; Li, Q.L.; Guo, Z.H.; Huang, Y.L. Methane-rich fluid inclusions and their hosting volcanic reservoir rocks of the Songliao Basin, NE China. *J. Geosci. Res. NE Asia* **2004**, *2*, 136–142.
6. Wang, P.J.; Hou, Q.J.; Wang, K.Y.; Chen, S.M.; Cheng, R.H.; Liu, W.Z.; Li, Q.L. Discovery and significance of high CH4 primary fluid inclusions in reservoir volcanic rocks of the Songliao Basin, NE China. *Acta Geol. Sin.* **2007**, *81*, 113–120.
7. Niu, J.Y.; Zhao, W.Z.; Zou, C.N.; Jiang, L.Z. Geologic features of the petroleum-rich sags in the Bohai Bay Basin. *Acta Geol. Sin.* **2008**, *82*, 636–642.
8. Zou, C.N.; Zhu, R.K.; Zhao, W.Z.; Jia, C.Z.; Zhang, G.Y.; Yuan, X.J.; Zhao, X.; Wen, B.H. Geologic characteristics of volcanic hydrocarbon reservoirs and exploration directions in China. *Acta Geol. Sin. (Engl. Ed.)* **2010**, *84*, 194–205. [CrossRef]
9. Zhu, D.Y.; Meng, Q.Q.; Jin, Z.J.; Hu, W.X. Thermodynamic analysis under influence for carbonate dissolution-filling of CO_2-rich deep fluid. *Chin. J. Geol.* **2012**, *47*, 187–201.
10. Sun, Y.H.; Kang, L.; Bai, H.F.; Fu, X.F.; Hu, M. Fault systems and their control of deep gas accumulations in Xujiaweizi area. *Acta Geol. Sin. (Engl. Ed.)* **2012**, *86*, 1547–1558.
11. Chen, Z.H.; Wang, X.L.; Zha, M.; Zhang, Y.Q.; Cao, Y.C.; Yang, D.S.; Wu, K.Y.; Chen, Y.; Yuan, G.H. Characteristics and formation mechanisms of large volcanic rock oil reservoirs: A case study of the Carboniferous rocks in the Kebai fault zone of Junggar Basin, China. *AAPG Bull.* **2016**, *100*, 1586–1617. [CrossRef]
12. Liu, X.H.; Feng, M.Y.; Xi, A.H.; Xiong, Y.X.; Dong, B.; Zhao, M.; Duan, H.J. Formation and evolution of the reservoir space of subvolcanic reservoir: A case study of the well Dixi 18 area in Kelameili Gasfield. *Nat. Gas Geosci.* **2016**, *27*, 278–288.
13. Ameen, M.S.; MacPherson, K.; Al-Marhoon, M.I.; Rahim, Z. Diverse fracture properties and their impact on performance in conventional and tight-gas reservoirs, Saudi Arabia: The Unayzah, South Haradh case study. *AAPG Bull.* **2012**, *96*, 459–492. [CrossRef]
14. Reiners, P.W.; Chan, M.A.; Evenson, N.S. (U-Th)/He geochronology and chemical compositions of diagenetic cement, concretions, and fracture-filling oxide minerals in Mesozoic sandstones of the Colorado Plateau. *Geol. Soc. Am. Bull.* **2014**, *126*, 1363–1383. [CrossRef]
15. Li, Y.T.; Zhang, S.N.; Han, J.; Cao, Z.C.; Huang, C.; Ye, N. Geochemical Characteristics Differences and Implication of the Reservoir of the Calcite Filling in the Middle-Lower Ordovician, Northern Slope of Tazhong Area. *Geol. Sci. Technol. Inf.* **2018**, *37*, 37–45.
16. Cui, J.D.; Zhang, J.Z.; Zhang, H.Y. Features of the Carboniferous Volcanic Rocks Fracture Reservoirs in Hongshanzui Oilfield, Junggar Basin. *J. Earth Sci.* **2013**, *24*, 997–1007. [CrossRef]
17. Felice, S.L.; Montanari, D.; Battaglia, S.; Bertini, G.; Gianelli, G. Fracture permeability and water-rock interaction in a shallow volcanic groundwater reservoir and the concern of its interaction with the deep geothermal reservoir of Mt. Amiata, Italy. *J. Volcanol. Geotherm. Res.* **2014**, *284*, 95–105. [CrossRef]
18. Zhao, W.Z.; Zou, C.N.; Li, J.Z.; Feng, Z.Q.; Zhang, G.Y.; Hu, S.Y.; Kuang, L.C.; Zhang, Y. Comparative study on volcanic hydrocarbon accumulations in western and eastern China and its significance. *Pet. Explor. Dev.* **2009**, *36*, 1–11.
19. Liu, G.Y.; Zhang, L.P.; Jin, Z.J. Primary study on the effects of deep source fluid's movement on hydrocarbon migration. *Pet. Geol. Exp.* **2005**, *27*, 269–275.
20. Mao, Z.G.; Zou, C.N.; Zhu, R.K.; Guo, H.L.; Wang, J.; Tang, Y.; Qi, L.Q.; Zhang, Z.G. Geochemical characteristics and tectonic settings of Carboniferous volcanic rocks in Junggar Basin. *Acta Petol. Sin.* **2010**, *26*, 207–216.
21. Xiong, Y.X.; Xi, A.H.; Ran, Q.Q.; Ge, Y.H.; Liu, X.H.; Sun, Y.H. Characteristics and significance of Carboniferous volcanic rocks in Dinan uplift. *Lithol. Reserv.* **2011**, *23*, 62–68.

22. Hou, L.H.; Zou, C.N.; Liu, L.; Wen, B.H.; Wu, X.Z.; Wei, Y.Z.; Mao, Z.G. Geologic essential elements for hydrocarbon accumulation within Carboniferous volcanic weathered crusts in northern Xinjiang, China. *Acta Pet. Sin.* **2012**, *33*, 533–540.
23. Zhang, F.; Xu, T.; Fan, J.J.; Pan, A.J.; Wang, B.; Chao, Y.Y. Whole-rock Sm-Ndisochron age of Carboniferous volcanic rocks in eastern Junggar and its tectonic significance. *Geochimica* **2014**, *43*, 301–316.
24. Zhao, H.L.; Wang, C.; Liu, Z.W.; Sun, W.L.; Qing, Z.; Chen, L.; Zhu, F. Characteristics of petrology and thermodynamics of selective dissolution of plagioclase in volcanic reservoir rocks. *Geol. Bull. China* **2009**, *28*, 412–419.
25. Liu, X.H.; Feng, M.Y.; Xi, A.H.; Yan, X.R.; Wu, Y.; Liu, C. Diagenesis and pore evolution of Carboniferous volcanic reservoirs in Dixi area, Kelameili Gas Fied. *Lithol. Reserv.* **2016**, *28*, 38–48.
26. Rittmann, A. On the serial character of igneous rocks. *Egypt. J. Geol.* **1957**, *1*, 23–48.
27. Fairchild, I.J.; Spiro, B. Petrological and isotopic implications of some contrasting late Precambrian carbonate, NE Spitsbergen. *Sedimentology* **1987**, *34*, 793–989. [CrossRef]
28. Wu, C.Z.; Gu, L.X.; Ren, Z.W.; Chen, Z.Y.; Zhai, M.; Qiu, J. Formation Mechanism of Hydrocarbon Reservoirs Related to Igneous Rocks in Mesozoic-Cenozoic Basin, Eastern China. *Acta Geol. Sin.* **2005**, *79*, 522–530.
29. Wu, C.Z.; Gu, L.X.; Zhang, Z.Z.; Ren, Z.W.; Chen, Z.Y.; Li, W.Q. Formation mechanisms of hydrocarbon reservoirs associated with volcanic and subvolcanic intrusive rocks: Examples in Mesozoic-Cenozoic basins of eastern China. *AAPG Bull.* **2006**, *90*, 137–147.
30. Burnham, C.W. Magmas and hydrothermal fluids. In *Geochemistry of Hydrothermal Ore Deposits*, 3rd ed.; Barnes, H.L., Ed.; John Wiley and Sons: New York, NY, USA, 1997; pp. 63–124.
31. Tan, J.Y.; Wang, S.F.; Wu, R.J.; Zhang, Y.Y.; Guo, Z.J. Types and time of Carboniferous volcanic edifices in eastern Junggar, Xinjiang. *Acta Petrol. Sin.* **2010**, *26*, 440–448.
32. Zeng, L.B.; Qi, J.F.; Wang, Y.X. Origin type of tectonic fractures and geological conditions in low-permeability reservoirs. *Acta Pet. Sin.* **2007**, *28*, 52–56.
33. Gu, L.X.; Wu, C.Z.; Ren, Z.W.; Chen, Z.Y.; Zheng, Y.C. Geological model for porphyry-type hydrocarbon reservoirs of the Liaohe oil field. *Sci. Online* **2007**, *2*, 500–504.
34. Guo, M.Z.; Wen, C.J.; Yuan, G.H.; Si, X.Q.; Zhu, G.H.; Wang, X. Features, origin and geological significance of geopetal structures in Carboniferous volcanic rocks in Niudong block, Santanghu Basin. *Mar. Orig. Pet. Geol.* **2010**, *15*, 74–78.
35. Hou, L.H.; Luo, X.; Wang, J.H.; Yang, F.; Zhao, X.; Mao, Z.G. Weathered volcanic crust and its petroleum geologic significance: A case study of the Carboniferous volcanic crust in northern Xinjiang. *Pet. Explor. Dev.* **2013**, *40*, 257–265. [CrossRef]
36. Gong, L.; Gao, S.; Fu, X.F.; Lyu, B.Y.; Yao, J.Q. Fracture characteristics and their effects on hydrocarbon migration and accumulation in tight volcanic reservoirs: A case study of the Xujiaweizi fault depression, Songliao Basin, China. *Interpretation* **2017**, *5*, 57–70. [CrossRef]
37. Chen, D.Z.; Chen, F.X. The application of the electron probe in the study of the alteration mineral halo. *Geoscience* **1996**, *2*, 130–138.
38. Tang, Y.; Zhang, H.; Liu, C.Q.; Rao, B. Geochemical behavior of phosphorus in the peraluminous magmatic-hydrothermal system. *Acta Petrol. Mineral.* **2008**, *27*, 127–134.
39. Jiang, S.C.; Chen, Y.M.; Pan, J. Experimental study on the impact of fluoride on phosphate minerals Ca^{2+}-$HPO_4{}^{2-}$-$HCO_3{}^{1-}$-F^{1-}-H_2O system. *Sci. Geol. Sin.* **1964**, *4*, 341–352.
40. Benmore, R.A.; Coleman, M.L.; Mcarthur, J.M. Origin of sedimentary francolite from its sulphur and carbon isotope composition. *Nature* **1983**, *302*, 516–518. [CrossRef]
41. Veizer, J.; Hoefs, J. The nature of $^{18}O/^{16}O$ and C^{13}/C^{12} secular trends in sedimentary carbonate rocks. *Geochim. Cosmochim. Acta* **1976**, *40*, 1387–1395. [CrossRef]
42. Taylor, H.P.; Frechen, J.; Degens, E.T. Oxygen and carbon isotope studies of carbonatites from the Laacher See district, West Germany and the Alno district, Sweden. *Geochimica Et Cosmochimica Acta* **1967**, *31*, 407–430. [CrossRef]
43. Hoefs, J. *Stable Isotope Geochemistry*, 4th ed.; Springer: Berlin, Germany, 1997; pp. 83–108.
44. Toyoda, K.; Horiuchi, H.; Tokonami, M. Dupalanomaly of Brazilian carbonatites: Geochemical correlations with hotspots in the South Atlantic and implications for the mantle source. *Earth Planet. Sci. Lett.* **1994**, *126*, 315–331. [CrossRef]

45. Cao, J.; Hu, W.X.; Yao, S.P.; Zhang, Y.J.; Wang, X.L.; Zhang, Y.Q.; Huang, Z.J. Carbon, oxygen and strontium isotope composition of calcite veins in the Carboniferous to Permian source sequences of the Junggar Basin: Implications on petroleum fluid migration. *Acta Sedimentol. Sin.* **2007**, *25*, 722–729.
46. Friedman, I.; O'Neil, J.R. Composition of stable isotopic fractionation factors of geochemical interest. In *Data of Geochemistry*; 6th U.S. Geological Survey: Professional Paper; Fleisher, M., Ed.; US Government Printing Office: Washington, DC, USA, 1977; Volume 440, pp. 1–12.
47. Palmer, M.R.; Elderfield, H. Sr isotope composition of sea water over the past 75Myr. *Nature* **1985**, *314*, 526–528. [CrossRef]
48. Da, J.; Hu, Y.; Zhao, M.J.; Song, Y.; Xiang, B.L.; Qin, S.F. Features of source rocks and hydrocarbon pooling in the Kelameiligasfield, the Junggar Basin. *Oil Gas Geol.* **2010**, *31*, 187–192.
49. Willkinson, M.; Haszeldine, R.S.; Ellam, R.M.; Fallick, A. Hydrocarbon filling timing history from diagenetic evidence: Brent Group, UK, North Sea. *Mar. Pet. Geol.* **2004**, *21*, 443–455. [CrossRef]
50. Lai, X.Y.; Yu, B.S.; Chen, Y.Y.; Chen, X.L.; Liu, J.Q.; Mei, M.X.; Jin, W.G.; Cheng, S.H. Clastic particles dissolved skeleton thermodynamic conditions in Kela 2 gas field and its application. *Sci. China Ser. D Earth Sci.* **2004**, *42*, 45–53.
51. Huang, K.K.; Huang, S.J.; Tong, H.P.; Liu, L.H. Thermodynamic calculation of feldspar dissolution and its significance on research of clastic reservoir. *Geol. Bull. China* **2009**, *28*, 474–482.
52. Peng, H.J.; Wang, X.W.; Tang, J.X.; Wang, D.H.; Qin, Z.P.; Hou, L.; Zhou, Y. The application of quartz cathodoluminescence in study of igneous rock. *Rock Miner. Anal.* **2010**, *29*, 153–160.
53. Chen, X.D.; Chen, Z.Y.; Cheng, Y.B.; Ye, H.S.; Wang, H. Distribution and application of trace elements in hydrothermal quartz: Understanding and prospecting. *Geol. Rev.* **2011**, *57*, 707–717.